Transient formation of bcc crystals in suspensions of poly(*N*-isopropylacrylamide)-based microgels

U. Gasser*
Laboratory for Neutron Scattering, Paul Scherrer Institut, 5232 Villigen PSI, Switzerland

J.-J. Lietor-Santos
School of Physics, Georgia Institute of Technology, Atlanta, Georgia 30332-0430, USA

A. Scotti
Laboratory for Neutron Scattering, Paul Scherrer Institut, 5232 Villigen PSI, Switzerland

O. Bunk and A. Menzel
Swiss Light Source, Paul Scherrer Institut, 5232 Villigen PSI, Switzerland

A. Fernandez-Nieves
School of Physics, Georgia Institute of Technology, Atlanta, Georgia 30332-0430, USA
(Received 1 July 2013; published 13 November 2013)

We present a small-angle x-ray scattering study of crystals formed by temperature-sensitive, swollen microgel particles consisting of poly(*N*-isopropylacrylamide) copolymerized with acrylic acid and 5 mol % of a cross-linker. As for hard spheres, the random hexagonal close-packed structure is predominant during crystal growth and slowly transforms toward the face-centered-cubic structure. However, a transient phase of body-centered-cubic crystal is observed in an intermediate range of effective volume fractions. We estimate that the studied suspensions are close to a transition from face-centered-cubic to body-centered-cubic structure that can be understood by the tendency of the system to maximize the excluded volume and minimize the contact area between the particles.

DOI: 10.1103/PhysRevE.88.052308 PACS number(s): 82.70.−y, 64.70.dg

I. INTRODUCTION

Microgels are cross-linked polymer particles with diameters in the nm and μm range that respond reversibly to changes in the environmental conditions by changing their size. This responsiveness is due to variations in polymer solubility, as induced by changes in temperature [1], hydrostatic pressure [2], pH [3], salt concentration [4], or external osmotic pressure [5]. This transition between swollen and deswollen states [6] is attractive for many applications [7–9] and also for studying the effect of particle softness on phase transitions such as crystallization.

As both the colloidal and polymeric properties of the particles are relevant for the behavior of microgel suspensions at high concentrations [10], their phase behavior is not as well understood as that of hard particles, and the interaction between microgel particles and the dependence on particle concentration is still not known in detail [11]. Recent work suggests that microgel particles interact via a Hertzian potential for center-to-center distances slightly below the particle diameter [12,13], although other works find that this potential does not provide a good model for the phase behavior of microgels [14]. From a theoretical point of view, charged microgels interacting via a Yukawa pair potential for center-to-center distances above the particle diameter and via a soft potential for distances below the particle diameter are predicted to form crystal structures which are different from those formed by hard-sphere suspensions at sufficiently high volume fractions [15]. However, our previous neutron and x-ray scattering studies on charged microgels [16,17] as well as experimental results by other groups [18,19] indicate that the crystal structure is comparable to that of hard spheres even for very dense packing, where particles have to deform and/or interpenetrate.

We present data from a small-angle x-ray scattering (SAXS) study of crystal growth in a slightly charged microgel system of poly(*N*-isopropylacrylamide) (pNIPAM) copolymerized with acrylic acid (AAc). As a result, in addition to the response to temperature changes by virtue of the pNIPAM, these particles are also pH sensitive, as AAc gets ionized at $p\mathrm{H} > 4.3$ [20]. We study suspensions at a fixed pH a little above this transition, such that the particles are slightly charged and show a clear temperature response. As in hard spheres, we find that random hexagonal-close-packed (rhcp) crystals grow initially. This is a random sequence of close-packed hexagonal planes that can be understood as a random mixture of the packing found in the face-centered-cubic (fcc) and the hexagonal-close-packed (hcp) lattice. The appearance of rhcp crystal shows that the free-energy difference between fcc and hcp lattices is small, as observed in hard spheres [21,22]. Furthermore, the rhcp crystal is found to transform slowly toward the fcc crystal lattice, which appears to be the equilibrium structure, as in hard spheres [22,23]. However, at intermediate volume fractions, a body-centered-cubic (bcc) crystal phase appears, which is not stable and, therefore, disappears as the samples age. This crystal structure is expected for hard-core Yukawa particles with an intermediate screening length and at volume fractions below those where the fcc structure is the ground state of the system [24]. In contrast, for fuzzy particles with a steric repulsion the bcc structure is not expected at low volume

*urs.gasser@psi.ch

fractions but is predicted to appear in an intermediate range of volume fractions, between a loosely and a densely packed fcc phase [25,26]. In analogy to this model, we observe the transient bcc crystal phase between bands of crystal with rhcp crystal that slowly converts to fcc. This suggests that our observations could be related to the predictions of the model for fuzzy particles. Our observations are also the first of this type for a microgel suspension.

II. EXPERIMENTAL METHODS

A. pNIPAM-AAc suspensions

We study temperature-sensitive particles consisting of poly(*N*-isopropylacrylamide) copolymerized with acrylic acid (2 mol %) and cross-linked with methylene-bis-acrylamide (5 mol %). As the cross-linker reacts faster than the NIPAM monomer during polymerization, the particles have a decaying concentration of cross-linker from the center to the periphery. The particles were synthesized as described in Refs. [27,28]. Their swelling behavior at $p\mathrm{H} = 4.5$ was determined by dynamic light scattering measurements; the particles show a broad volume transition between 25 and 40 °C, with a hydrodynamic radius that decreases from $R_h = (159 \pm 7)$ nm at 20 °C to (63 ± 2) nm at 50 °C, as shown in Fig. 1. The volume phase transition is broader than in pure pNIPAM microgel particles due to the slight charge of the AAc groups. Viscometry measurements were carried out with dilute suspensions at $p\mathrm{H} = 4.5$ and 24 °C, which corresponds to a swollen particle state, to relate the polymer concentration, c_p, to the generalized volume fraction, ζ, according to the Batchelor-Einstein equation [29]. We obtain $\zeta = kc_p$, with a conversion factor $k = 0.241$ wt. %$^{-1}$.

The phase behavior of suspensions with polymer concentrations in the range from $c_p = 1.0$ wt. % ($\zeta = 0.24$) up to $c_p = 6.9$ wt. % ($\zeta = 1.66$) was inspected visually (Fig. 2). Crystallization was observed in the range from $c_p = 1.90$ wt. % ($\zeta = 0.46$) to $c_p = 2.54$ wt. % ($\zeta = 0.61$) and a series of eight suspensions in this range was prepared for SAXS measurements. To obtain an overview of the crystallization and crystal structure with time, samples in quartz capillaries were prepared 26, 19, 12, 6, and 2 days, as well as 21 and 2 h before

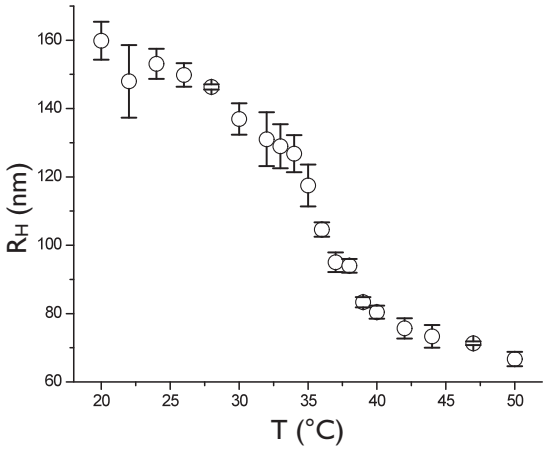

FIG. 1. Hydrodynamic radius of pNIPAM-AAc particles at $p\mathrm{H} = 4.5$, determined by dynamic light scattering, vs temperature.

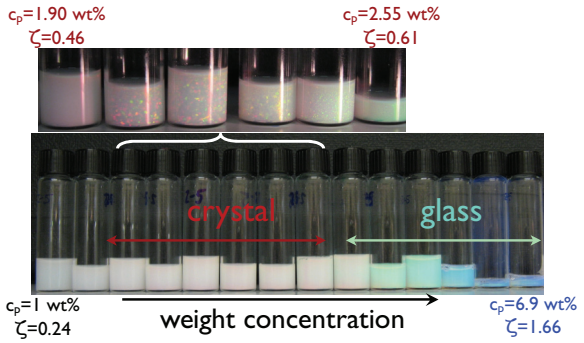

FIG. 2. (Color online) Phase behavior of pNIPAM-AAc microgel particles at $p\mathrm{H} = 4.5$ as determined by visual inspection. The opal-like appearance of the crystal samples is due to Bragg peaks observed with visible light.

the start of the SAXS measurements. All measurements were carried out in the fully swollen state at 24 °C. In addition, a series of samples was heated up to 41 °C to melt the crystals and cooled back down to 24 °C. The subsequent recrystallization was monitored for 12 h.

B. SAXS

All samples were measured on the cSAXS beamline of the Swiss Light Source at Paul Scherrer Institut, Switzerland. The instrument was set up for a wavelength of 0.1425 nm and a sample-to-detector distance of 7.12 m to measure the signal at low values of the scattering vector $q = (4\pi/\lambda)\sin(\theta/2)$, where λ is the wavelength and θ is the scattering angle. The two-dimensional (2D) detector has a pixel size of 172 μm [30] and the beam was collimated to illuminate an area of $\approx 200 \times 200$ μm^2 on the sample. The samples were loaded in quartz capillaries with an inner diameter of 1 mm and centered in the beam with a series of short measurements. Measurements were taken in several locations along the sample capillary to obtain an overview of the phase behavior of the sample. Typically, data sets of 20 measurements of 0.1 s each were taken with the 2D detector. The observed Bragg peaks were found to be diminished by the x-ray beam after ≈ 0.5 s probably due to local heating. For this reason, only the first 0.4 s of the measurements was used for the analysis of the observed crystals. Since the particle diameter is ≈ 270 nm, only the region of 500×500 pixels close to the direct beam was of interest for determining the form factor and the crystal structure ($0.01 < q < 0.2$ nm^{-1}); all the presented analysis is done with this central part of the detector.

III. RESULTS AND DISCUSSION

The particle form factor, $P(q)$, was measured with a dilute sample at $c_p \approx 0.01$ wt. % ($\zeta \approx 0.0024$). The obtained scattering profile, shown in Fig. 3(a), was analyzed using the form-factor model of Stieger and Richtering [31,32]. We used the same form-factor model in earlier small-angle neutron-scattering measurements carried out with the same type of particles [33]. Within this model, the particle consists of a compact core, treated as a hard sphere, and a fuzzy

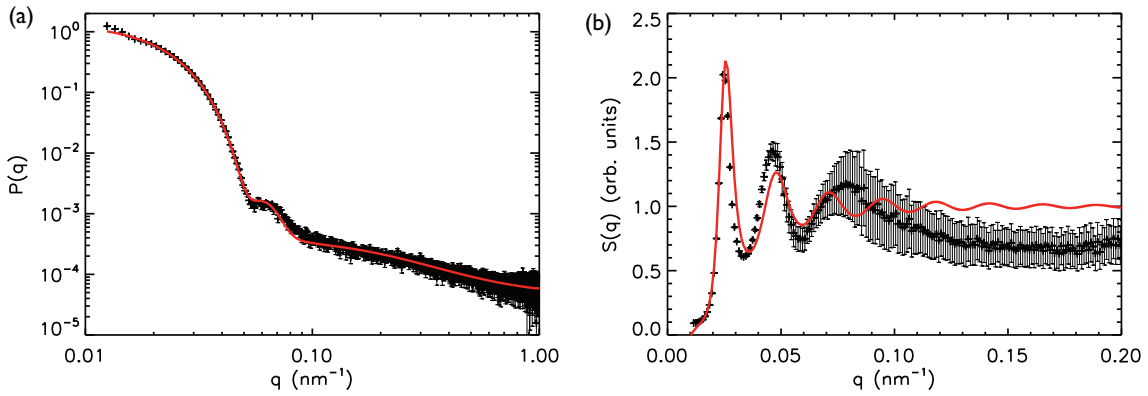

FIG. 3. (Color online) (a) SAXS measurement of the particle form factor taken with a sample at $c_p \approx 0.01$ wt. % ($\zeta \approx 0.0024$). The red line shows the fit obtained with the form-factor model of Stieger and Richtering; see text for details. (b) (Symbols) Structure factor of a fluid sample at $c_p \approx 1.90$ wt. % ($\zeta = 0.46$) compared with (red line) the Percus-Yevick structure factor.

corona of polymer strands sticking out into the solvent that is accounted for by convoluting the spherical core with a Gaussian with variance σ^2. In reciprocal space, the form factor, $P_1(q)$, is obtained as the form factor of a sphere with radius R and constant scattering length density representing the core multiplied by a Gaussian with variance $(1/\sigma)^2$:

$$P_1(q) = \left[\frac{3(\sin qR - qR\cos qR)}{(qR)^3}\exp[-(\sigma q)^2/2]\right]^2. \quad (1)$$

We also account for core polydispersity with a Gaussian size distribution of width $\sigma_{\rm pol}$,

$$D(R) = \frac{1}{\sqrt{2\pi}\sigma_{\rm pol}R_{\rm av}}\exp\left[-\frac{(R-R_{\rm av})^2}{2\sigma_{\rm pol}^2R_{\rm av}^2}\right]. \quad (2)$$

Inhomogeneities inside the cross-linked pNIPAM-AAc particles also contribute to the form factor. Their correlation length is expected to correspond to the mesh size, ξ, of the polymer. This can be estimated from the number of particles, N_p, the volume of one particle, V_p, and the number of cross-linker molecules, $N_{\text{x-link}}$, in the sample: $\xi = (N_p\,V_p/N_{\text{x-link}})^{1/3} \approx 5$ nm. A Lorentzian term is, therefore, added to the form factor: $I_{\rm chain}(q) = I_{\rm chain}(0)/[1+(\xi q)^2]$. The complete expression for the form-factor model is given by

$$P(q) = \int_0^\infty dR\,D(R)P_1(q) + I_{\rm chain}(q). \quad (3)$$

From the fit we obtain the values for the core radius, $R_{\rm av} = (89.2 \pm 0.6)$ nm, the fuzzy shell size, $\sigma = (21.9 \pm 0.6)$ nm, and the polydispersity, $\sigma_{\rm pol} = 0.096 \pm 0.006$. The total particle radius is obtained as $R_{\rm SAXS} = R_{\rm av} + 2\sigma = (133.1 \pm 1.8)$ nm. This is smaller than the hydrodynamic radius $R_h = (152 \pm 7)$ nm obtained at 24 °C, possibly due to the hardly detectable contribution of the outskirts of the fuzzy particle corona to the SAXS intensity.

The form factor is used to obtain the structure factor $S(q) = I(q)/P(q)$, with $I(q)$ the scattered intensity of the investigated crystal samples. Figure 3(b) shows a comparison of the structure factor obtained for a sample at $\zeta = 0.46$ in the supercooled fluid state with the corresponding Percus-Yevick (PY) structure factor [34]. The measured $S(q)$ was multiplied by a factor to fit the height of the first peak of the PY structure factor. The positions of the first and second peak agree with PY expectations. However, there is a clear disagreement at high q, which may be due to the errors in the form-factor measurement for $q > 0.08$ nm^{-1} [see Fig. 3(a)] and their propagation when obtaining $S(q)$.

The initial evolution of the samples was followed with capillaries that were filled right before the measurement. The time taken for crystals to appear was determined by performing measurements at times between those mentioned in the previous section; they are listed in Table I. The samples with intermediate effective volume fraction in the range $0.5 < \zeta < 0.6$ were found to crystallize within a few hours, while those with lower or higher ζ took considerably longer. This behavior is analogous to that expected from hard spheres, where the fastest nucleation density rates, J, are observed close to the melting point at volume fraction $\phi_m = 0.54$ at the upper end of the ϕ-range of crystal-fluid coexistence [35]. The driving force for nucleation, given by the difference of the chemical potentials of the fluid and the crystal state, $\Delta\mu$, increases with volume fraction and, therefore, J is also expected to increase. However, J reaches a maximum, as the kinetics of the incorporation of particles into crystal nuclei is slowed down [36]. Moreover, a simulation study of hard spheres indicates that the surface tension, γ, of the crystal-fluid interface of hard spheres depends on $\Delta\mu$ such that the free-energy barrier for nucleation increases for $\phi \gtrsim \phi_m$ and causes J to decrease [37].

In all studied samples, the random hexagonal close-packed (rhcp) lattice is found to form from fluid states obtained either by shear-melting crystals while filling the capillaries or by heating the sample to 41 °C followed by cooling down to the swollen state at 24 °C. Bragg rings with peak positions expected for rhcp crystal are observed in many samples; an example is shown in Fig. 4(a). A hexagonal pattern of Bragg reflections is also observed in many samples, as shown in Fig. 4(b); this suggests the formation of hexagonal crystal layers on the wall of the sample capillary by heterogenous nucleation such that hexagonal planes are oriented perpendicular to the x-ray beam. This behavior is analogous to hard spheres, which spontaneously form rhcp crystal on a flat wall, as the wall strongly reduces the free-energy barrier for crystal nucleation [38].

TABLE I. The effective volume fraction, ζ, polymer concentration, c_p, rhcp lattice parameter a (nearest-neighbor distance), time for crystallization, and the dominant crystal structure observed in the youngest and the oldest crystalline samples for all studied samples, together with the parameter α [Eq. (4)] giving the randomness of the rhcp crystal. As samples were remeasured in irregular intervals, only a rough estimate of the crystallization time can be given.

	c_p (±0.005)	a_{hcp} (±2)	t_{crystal}	crystal structure, α (±0.05)	
ζ (±0.005)	(% wt.)	(nm)	(h)	early	final
0.460	1.900	320	14 ± 9	rhcp 0.50	rhcp 0.65
0.480	2.000	317	14 ± 9	rhcp 0.50	rhcp 0.60
0.510	2.110	302	2.5 ± 1	rhcp 0.50/bcc	rhcp 0.60
0.520	2.180	297	2.5 ± 1	rhcp 0.50/bcc	rhcp 0.70
0.540	2.250	295	2.5 ± 1	rhcp 0.60/bcc	rhcp 0.65
0.570	2.350	292	0.5 ± 0.5	rhcp 0.50/bcc	rhcp 0.70
0.590	2.460	289	2.5 ± 1	rhcp 0.58	rhcp 0.63
0.610	2.550	283	30 ± 10	rhcp 0.60	rhcp 0.72

The structure factor of rhcp crystal, $S_{\mathrm{rhcp}}(\boldsymbol{q})$, is given by Bragg peaks and Bragg rods, which are due to the random stacking of hexagonal planes sketched in Fig. 4(c). The Bragg rods are oriented perpendicular to the hexagonal planes, along the direction of random stacking, the q_z direction in Fig. 4(d). The positions of the Bragg rods and Bragg peaks in the (q_x,q_y) plane are given by the Bragg peaks of a single hexagonal plane, and the intensity variation along the rods (q_z direction) is given by a continuous intensity variation depending on the randomness of the stacking of the hexagonal planes. The condition for Bragg peaks is fulfilled for the second Bragg ring [green dots in Fig. 4(d)], while Bragg rods are observed for the first and third rings in Fig. 4(d). Close packing of hexagonal planes allows for three different positions of the planes, labeled A, B, and C in Fig. 4(c). Two neighboring hexagonal planes are, therefore, always shifted by either $\boldsymbol{r}_1$ or $\boldsymbol{r}_2$, also shown in Fig. 4(c). The sequence of the hexagonal plane positions is random in rhcp crystal. This randomness is measured by the parameter α: given that the shift from a first to a second hexagonal plane is given by translation vector $\boldsymbol{r}_1$, α gives the probability that the shift from the second to the third plane is also given by $\boldsymbol{r}_1$. Thus, $\alpha = 0$ corresponds to an alternating stacking with translation vectors $\boldsymbol{r}_1$ and $\boldsymbol{r}_2$ giving, e.g., the sequence $AB\,AB\,AB\,\ldots$ of the hexagonal planes sketched in Fig. 4(c). Therefore, the hexagonal close-packed (hcp) lattice is obtained with $\alpha = 0$, while $\alpha = 1$ corresponds to the face-centered-cubic (fcc) lattice with the stacking $ABC\,ABC\,\ldots$. A completely random stacking is given by $\alpha = 1/2$. The variation of the structure factor along the stacking direction given by $\hat{\boldsymbol{q}}_z$ was determined as a function of α in Ref. [39]; an earlier treatment of the problem is found in Ref. [40]. The result is

$$\begin{aligned} S_{\mathrm{rhcp}}(\boldsymbol{q}) = {} & S_{\mathrm{hex}}(q_x,q_y)\,\alpha(1-\alpha)\{1-\cos[\boldsymbol{q}\cdot(\boldsymbol{r}_1-\boldsymbol{r}_2)]\} \\ & /\{1-2\alpha+3\alpha^2-2\alpha^2[\cos(\boldsymbol{q}\cdot\boldsymbol{r}_1)+\cos(\boldsymbol{q}\cdot\boldsymbol{r}_2)] \\ & +\alpha^2\cos[\boldsymbol{q}\cdot(\boldsymbol{r}_1-\boldsymbol{r}_2)] \\ & +(2\alpha-1)\cos[\boldsymbol{q}\cdot(\boldsymbol{r}_1+\boldsymbol{r}_2)]\}, \end{aligned} \tag{4}$$

where $S_{\mathrm{hex}}(q_x,q_y)$ is the structure factor of one hexagonal plane in two dimensions, which, therefore, only depends on q_x and q_y. Equation (4) is valid for the first and third ring of Bragg rods [red and blue dots in Fig. 4(d)]. However, it does not apply for the second ring, where the condition for Bragg peaks, $\exp[i\boldsymbol{q}\cdot\boldsymbol{r}_1] = \exp[i\boldsymbol{q}\cdot\boldsymbol{r}_2]$, is fulfilled and the denominator of Eq. (4) always vanishes. In this case, Eq. (4) becomes [39]

$$S_{\mathrm{rhcp}}(\boldsymbol{q}) = S_{\mathrm{hex}}(q_x,q_y)\,\frac{1}{M}\,\frac{\sin^2[(M/2)\boldsymbol{q}\cdot\boldsymbol{r}_1]}{\sin^2[(1/2)\boldsymbol{q}\cdot\boldsymbol{r}_1]}, \tag{5}$$

where M is the number of hexagonal planes that are stacked on top of each other and is a measure of the sharpness of the Bragg peaks. For crystallization in the bulk, samples are expected to be polycrystalline, as crystal grains nucleate with random orientations. Therefore, we calculate the radial average of $S_{\mathrm{rhcp}}(\boldsymbol{q})$ with a probability distribution $p[\cos(\theta)] = 1/(4\pi)$ for $-1 < \cos(\theta) \leqslant 1$, where θ is the angle between the Bragg rods and the incident beam direction $\hat{\boldsymbol{k}}_i$; hence, $\cos(\theta) = \hat{\boldsymbol{q}}_z \cdot \hat{\boldsymbol{k}}_i$. The resultant structure factor is

$$\begin{aligned} & S_{\mathrm{poly-rhcp}}(q) \\ & \quad = F_{\mathrm{DW}}(q)\int_0^{2\pi} d\phi \int_0^{\pi} d\theta\,\sin(\theta)\,p[\cos(\theta)]\,S_{\mathrm{rhcp}}(\boldsymbol{q}), \end{aligned} \tag{6}$$

where we have included a Debye-Waller factor, $F_{\mathrm{DW}}(q) = \exp(-q^2\langle u^2\rangle/3)$, to take into account local particle fluctuations. The average displacement of the particles is set to $\langle u\rangle = 0.1a$, where a is the lattice constant. The angles θ and ϕ are polar coordinates of $\boldsymbol{q} = q\,[\sin(\theta)\,\cos(\phi), \sin(\theta)\,\sin(\phi), \cos(\theta)]$, and the direction of the Bragg rods is assumed to be given by $\hat{q}_z = (0,0,1)$. As mentioned above, hexagonal patterns of Bragg peaks are observed in many samples, which is expected for heterogeneous crystallization on the capillary walls. In these cases, the choice $p[\cos(\theta)] = \delta[\cos(\theta)-1]$, corresponding to $\theta = 0$, usually gives a good fit to the measured $S(q)$.

The structure factor of the crystal appearing after sample preparation can be described with a stacking probability $\alpha \approx 0.5$, as shown in Figs. 4(e) and 4(f). The rhcp crystal lattice accounts for all peaks, and the intensities of the first two peaks are well reproduced. Lorentzian curves are used for the fits, as with this peak shape we reproduce the background caused by disorder within and between crystal grains to some extent. The peak width at half-maximum is approximated as $\Delta q \approx 0.06q$, which is comparable but slightly larger than the q resolution of the instrument. The resolution is given by

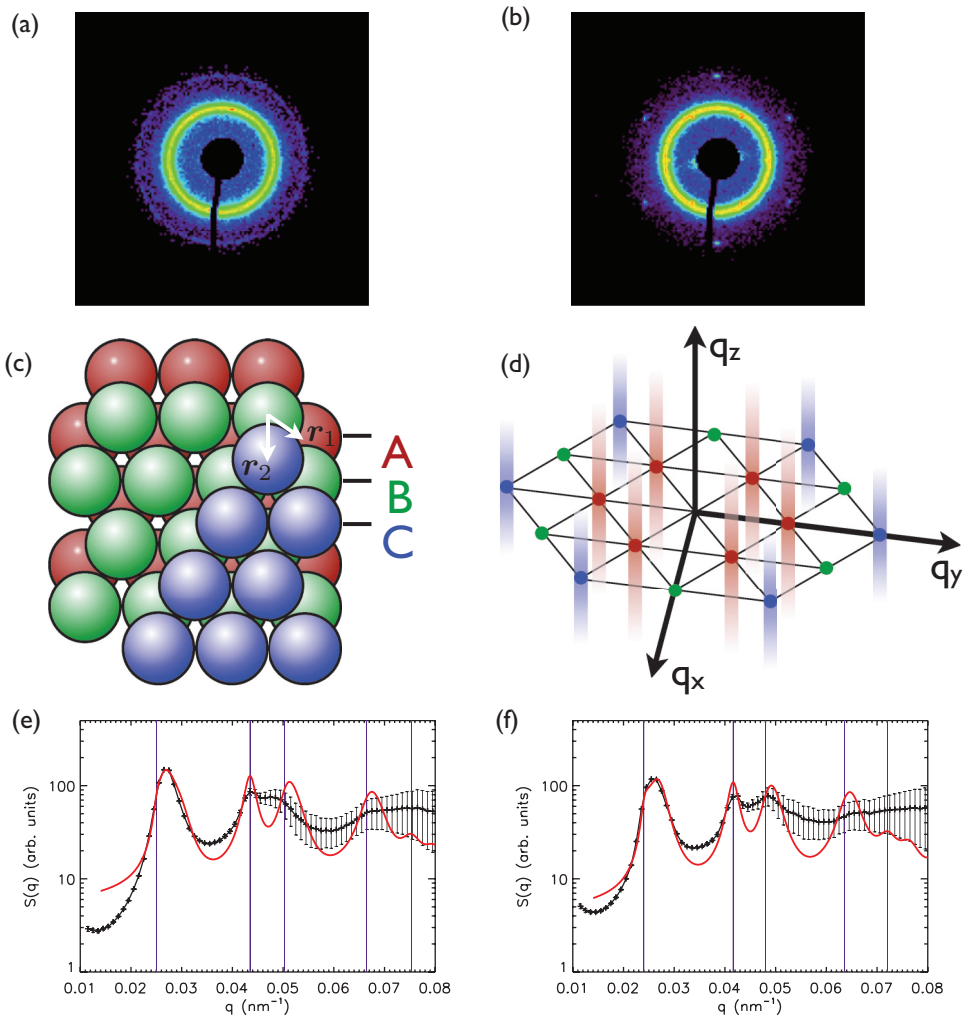

FIG. 4. (Color online) (a,b) Detector images taken at (a) $\zeta = 0.61$ with Bragg rings and (b) $\zeta = 0.59$ with a hexagonal pattern of Bragg peaks. (c) The three stacking positions A, B, and C for hexagonal particle planes for close-packed crystals. See text for details. (d) Sketch of the scattering intensity in $\boldsymbol{q}$ space obtained from a rhcp lattice. The reciprocal-lattice points of the hexagonal plane are highlighted by dots, and Bragg rods are shown by fading vertical bars. (e,f) Azimuthally averaged structure factor of rhcp crystals formed in young samples with (e) $a_{\mathrm{rhcp}} = (289 \pm 2)$ nm, $\alpha = 0.60 \pm 0.05$, $\zeta = 0.61$ prepared ≈ 2 h before the measurement and (f) $a_{\mathrm{rhcp}} = (302 \pm 2)$ nm, $\alpha = 0.50 \pm 0.05$, $\zeta = 0.51$ after melting with a temporary increase of temperature to 41 °C. The red curves represent the rhcp fits. The vertical lines show the Bragg peak positions of a single hexagonal plane.

$dq/q = d\theta/\theta + d\lambda/\lambda$, where θ is the scattering angle, and the wavelength spread $d\lambda/\lambda \approx 2 \times 10^{-4}$. The contribution $d\theta/\theta$ depends on the distance of a detector pixel from the direct beam position; for the first peak observed at $q \approx 0.026$ nm^{-1} we have $d\theta/\theta \approx 0.04$, and $d\theta/\theta \approx 0.025$ for the second peak at $q \approx 0.042$ nm^{-1}. As in the fluid sample above, the error in $S(q)$ increases considerably for $q > 0.04$ nm^{-1}, where the statistical error in the data increases due to the sharp dropoff of the form factor shown in Fig. 3(a). As rhcp crystals are a random mixture of fcc- and hcp-like packing of hexagonal planes, the observed formation of rhcp crystal shows that the free-energy difference between fcc and hcp crystal is small in the studied suspensions of pNIPAM-AAc particles. However, we find that older samples transform toward the fcc stacking, as shown in Fig. 5. The best fit to the measured $S(q)$ is obtained with $\alpha \approx 0.7$ for samples that have aged for 19 to 26 days. The fit in the figure (red line) includes the corresponding rhcp calculation. The shoulder on the right-hand side of the first peak at $q \approx 0.026$ nm^{-1} is a sign for fcc stacking, as the (1,1,1) and (2,0,0) reflections of fcc crystal appear at $q \approx 0.026$ nm^{-1} and $q \approx 0.030$ nm^{-1}, respectively, for a nearest-neighbor distance of 299 nm [Fig. 5(a)]. Again, the appearance of fcc crystal is analogous to the behavior of hard spheres, whose equilibrium crystal structure is given by the fcc lattice. The hard-sphere-like behavior may be due to the relatively high stiffness of the particles with a cross-linker concentration of 5 mol %, and softer particles might show a different behavior.

However, contrary to the hard-sphere-like behavior described above, an additional crystal structure is observed in several samples with concentrations in the range $0.50 < \zeta < 0.58$. This additional crystal structure is most probably body-centered-cubic (bcc) and appears together or somewhat after the appearance of the rhcp crystal. In older samples,

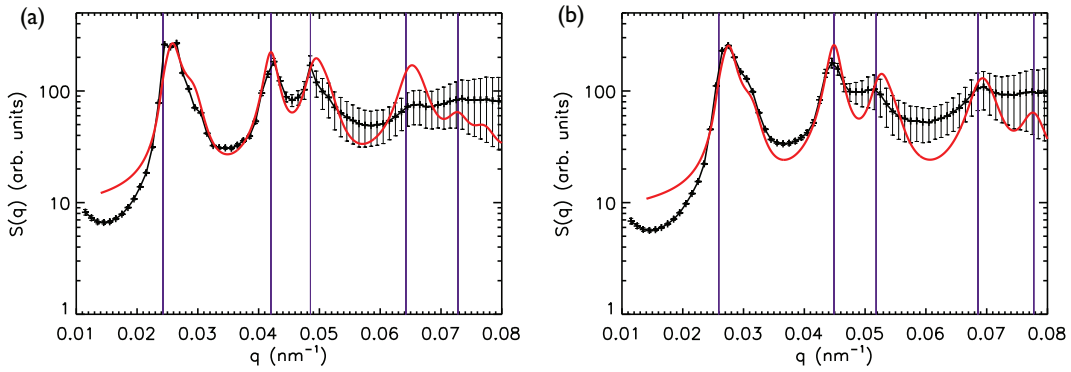

FIG. 5. (Color online) Azimuthally averaged structure factors $S(q)$ of crystal with predominant fcc stacking. (a) $a_{\mathrm{rhcp}} = (299 \pm 2)$ nm, $\zeta = 0.52, \alpha = 0.70 \pm 0.05$, and (b) $a_{\mathrm{rhcp}} = (280 \pm 2)$ nm, $\zeta = 0.61, \alpha = 0.72 \pm 0.05$. Both samples were prepared 26 days before the measurement. The red lines represent the rhcp fit. The vertical lines show the Bragg peak positions of a single hexagonal plane.

the bcc crystal phase is not observed, suggesting that this is not a stable phase of the studied pNIPAM-AAc particles. Our evidence for bcc crystal comes from two peaks in the radially averaged $S(q)$ curves and the 2D pattern of Bragg peaks visible in some samples, which cannot be obtained with fcc, hcp, or rhcp lattices with a particle density close to the one observed in the rhcp crystal. The sample with $\zeta = 0.57$ is an example of this type of behavior. The corresponding $S(q)$ taken 3.5 h after melting the sample with a temperature change to 41 °C is shown in Fig. 6(a). The peaks at $q \approx 0.039$ and 0.047 nm^{-1} can be accounted for with a bcc lattice, but not with the rhcp lattice that is found to coexist with the bcc crystal. Thus the red line in Fig. 6(a) represents a superposition of the scattering from a bcc and a rhcp lattice. We expect the particle densities in the bcc and the rhcp lattice to be about the same, as they coexist at constant osmotic pressure. From the observed peak positions, we obtain the lattice constants for the bcc lattice, $a_{\mathrm{bcc}} = (325 \pm 2)$ nm, and the rhcp lattice, $a_{\mathrm{rhcp}} = (289 \pm 2)$ nm. Recalling that there are two particles per conventional unit cell in either crystal structure, we obtain particle number densities of $n_{\mathrm{bcc}} = \frac{2}{a_{\mathrm{bcc}}^3} = (58.3 \pm 1.0)\ \mu\mathrm{m}^{-3}$ and $n_{\mathrm{rhcp}} = \frac{2}{\sqrt{2}a_{\mathrm{rhcp}}^3} = (58.6 \pm 1.2)\ \mu\mathrm{m}^{-3}$, which indeed agree with each other supporting the proposed coexistence of rhcp and bcc lattices. Furthermore, a set of Bragg peaks fitting a bcc lattice is observed in the 2D detector image of the same measurement, as shown in Fig. 6(b). The highlighted Bragg peaks fit the peaks expected from a bcc lattice with an incident beam along the (1, 1, 0) direction in the conventional unit cell of bcc. The (1,1,0) plane is the densest plane in the bcc lattice and its formation on the wall can therefore be expected. However, our time-resolved measurements show that the bcc crystal is not present in samples older than $\sim$ 10 h, suggesting that the system is close to coexistence of fcc and bcc, with the bcc lattice being only metastable. Evidence for the coexistence of fcc and bcc was found before in a light-scattering study [19], where only the first peak of the bcc crystal was observed.

We estimate the free energy of fcc and bcc crystal using the foam model for particles with a hard core surrounded by a soft corona [25,26]. The model relies on two competing effects controlling the crystal structure made by this kind of particle. On the one hand, the maximum packing fraction rule, at play in the presence of pure excluded-volume interactions,

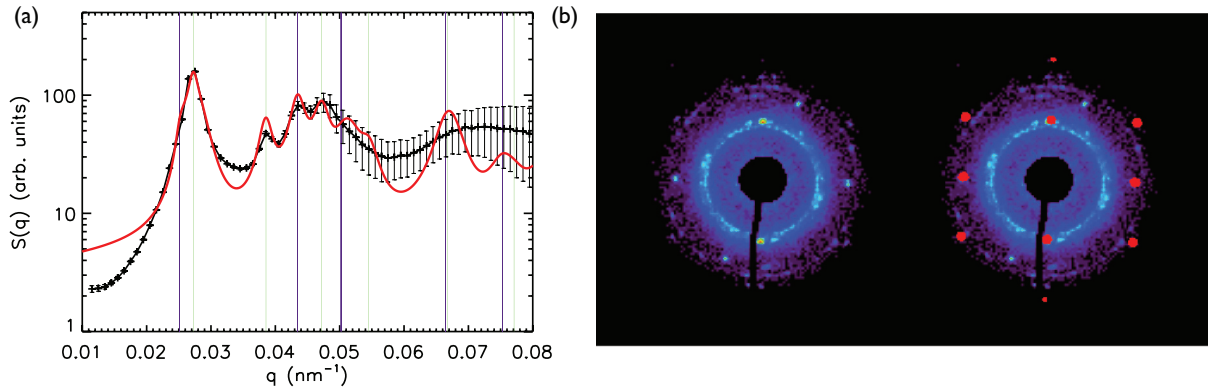

FIG. 6. (Color online) (a) Measured structure factor at $\zeta = 0.57$ showing peaks corresponding to rhcp and bcc crystals. The red curve shows the structure factor expected for a superposition of rhcp (45%), with $a_{\mathrm{rhcp}} = (289 \pm 2)$ nm, $\alpha = 0.5 \pm 0.05$, and bcc (55%) crystal, with $a_{\mathrm{bcc}} = (326 \pm 2)$ nm. The magenta vertical lines show the Bragg peak positions of a single hexagonal plane, while the green lines show bcc Bragg peak positions. (b) Detector image of the measurement shown in (a) with a logarithmic color scale. The original detector image is shown on the left, and the same image with the bcc-like Bragg peaks highlighted in red is shown on the right. The position of the bcc peaks is calculated with an incident beam direction $\boldsymbol{k}_i = (1,1,0)$ in the bcc reciprocal lattice.

favors a close-packed structure, as the configurational entropy of the system is maximum in this situation. On the other hand, the principle of contact area minimization, at play since the interaction between the particles scales with the contact area between them, favors the formation of more loosely packed structures such as the bcc or the A15 lattice, which is a bcc lattice with eight basis atoms in the unit cell. According to the foam model, the corresponding contributions to the system free energy are given by Eqs. (2) and (5) in Ref. [25]:

$$F^X_{\text{bulk}} = -k_B T \log\left[\alpha^X \left(\frac{\beta^X}{n^{1/3}} - 1\right)^3\right], \tag{7}$$

$$F^X_{\text{surface}} = \frac{l N_0 k_B T}{R} \frac{\gamma^X n^{-2/3}}{n^{-1} - 4\pi/3}, \tag{8}$$

where α^X, β^X, and γ^X, given in Table II, are geometrical constants for lattice $X \in \{\text{fcc}, \text{bcc}\}$, n is the particle number density, R is the total particle radius, and N_0 is the number of polymer strands in the corona of the particles. The parameter l is a length defining the overlap of two interacting particles and defines the strength of their steric repulsion.

We estimate N_0 from the fraction of polymer present in the corona according to the measured form factor. In real space, the polymer density of a particle, d_{polymer}, relative to the polymer density in the core, $d_{\text{polymer,core}}$, is given by the compact core convoluted with a Gaussian. This relative polymer density can be calculated as a function of the position, $\boldsymbol{r}$, for a particle with center of mass at $\boldsymbol{r} = \boldsymbol{0}$:

$$\begin{aligned}\frac{d_{\text{polymer}}(\boldsymbol{r})}{d_{\text{polymer,core}}} &= \frac{1}{(\sqrt{2\pi}\sigma)^3}\int_0^\infty dr'\, r'^2 \int_0^\pi d\theta\, \sin(\theta) \int_0^{2\pi} d\varphi\, \Theta(R_{\text{av}} - r')\, e^{-\frac{|r'-r|^2}{2\sigma^2}} \\ &= \frac{2\left(-e^{-\frac{(r-R_{\text{av}})^2}{2\sigma^2}} + e^{-\frac{(r+R_{\text{av}})^2}{2\sigma^2}}\right)\sigma - \sqrt{2\pi}\, r\, \text{Erf}\left[\frac{r-R_{\text{av}}}{\sqrt{2}\sigma}\right] + \sqrt{2\pi}\, r\, \text{Erf}\left[\frac{r+R_{\text{av}}}{\sqrt{2}\sigma}\right]}{2\sqrt{2\pi}\, r}\end{aligned} \tag{9}$$

with $\Theta(R_{\text{av}} - r')$ the Heaviside function representing the core and Erf the error function. Note that σ defines the width of the corona. From here, we can calculate the fraction of polymer contained in the corona as $4\pi \int_{R_{\text{av}}}^\infty dr\, r^2\, d_{\text{polymer}}(r)$. Using $R_{\text{av}} = (89.2 \pm 0.6)$ nm and $\sigma = (21.9 \pm 0.6)$ nm from the form-factor fit presented above, we estimate a fraction of polymer in the corona of ≈ 0.3. In addition, we estimate the number of polymer strands in the particle as $N_s \approx N_{\text{x-link}}$, where $N_{\text{x-link}}$ is the number of cross-linker molecules in a particle. Hence $N_s \approx x_{\text{BIS}}\, d_{\text{susp}}\, V_p/(k\, M) \approx 1.7 \times 10^5$, where we have used a value of the conversion constant, $k = 24.1$, a mass density of the suspension, $d_{\text{susp}} \approx 1.02$ g/cm^3, and an average molar mass per monomer, $M = 114.387$ g/mol, obtained from the molar masses of the monomers, $M_{\text{NIPAM}} = 113.158$ g/mol, $M_{\text{AAc}} = 72.063$ g/mol, and $M_{\text{BIS}} = 154.167$ g/mol, and the corresponding monomer molar fractions, $x_{\text{NIPAM}} = 0.93$, $x_{\text{AAc}} = 0.02$, and $x_{\text{BIS}} = 0.05$. The result is the number of polymer strands in the corona, $N_0 \approx 0.3\, N_s = 5.0 \times 10^4$.

To calculate the total free energy, we also need to know the overlap thickness, l, of the coronas of two interacting particles. This, however, is not known. As a result, we can only estimate F^X_{surface}. We do so by choosing an R in the range from $R_{\text{SAXS}} = (134.2 \pm 1.8)$ nm to $R_h = (152 \pm 7)$ nm, and an overlap thickness, l, between 0.5 and 15 nm. We then find that the total free energy of the bcc lattice is lower than that of the fcc lattice by 3–9 %, suggesting that the formation of a transient bcc structure in our microgel suspension could be related to the repulsion between the fuzzy outskirts of the particles and the natural tendency to reduce the associated surface free energy. Further support of this fact is that the formation of the transient bcc structure is only observed at intermediate ζ-values, consistent with the foam model expectation that this structure would form between an expanded and a compressed fcc structure. Despite this fact, we observe that the fcc structure is the one that prevails at all studied ζ, suggesting that the entropic contribution to the free energy resulting from the volume inaccessible for the center of mass of the particles' core dominates the total free energy of the system. In addition, we also note that the foam model may not have the correct balance between F_{bulk} and F_{surface}, as it uses generic expressions for the contributions to the free energy and does not take the details of the polymer density inside the microgel [Eq. (9)] into account.

TABLE II. Values of the geometrical factors α^X, β^X, γ^X, and the particle density, n, for F_{bulk} and F_{surface} according to the foam model [25]. See text for details.

lattice	α^X	β^X	γ^X	n (μm^{-3})
fcc	$2^{5/2}$	$2^{-5/6}$	5.345	58.6 ± 1.2
bcc	$2^2\sqrt{3}$	$2^{-5/3}\sqrt{3}$	5.306	58.3 ± 1.0

IV. CONCLUSIONS

The presented SAXS study shows that the fcc crystal structure is the equilibrium structure of suspensions of pNIPAM-AAc microgel particles with a 5 mol % cross-linker. Random hcp crystal forms spontaneously due to the small free-energy cost of having stacking faults of hexagonal crystal planes. This behavior is analogous to that of hard spheres and consistent with what was observed in suspensions of ionic vinyl-pyridine microgel suspensions [17]. However, the formation of bcc crystal we observe is incompatible with hard-sphere-like behavior and could result from the influence of an area-minimizing principle suggested by the foam model [25,26]. As the rhcp crystal, the bcc crystal appears to form predominantly by heterogeneous nucleation on the wall of the sample capillaries. We believe the bcc structure is metastable because it disappears as the samples age. Furthermore, it only forms within a certain ζ-range below and above which we only

observe the formation of rhcp crystal; this is also qualitatively consistent with the foam model, which predicts that indeed the bcc lattice is bounded between an expanded and a compressed fcc lattice. Studies of the phase behavior in dependence of the cross-linker concentration are needed to reach a more detailed understanding of the behavior of microgels and other soft particles and to quantitatively assess whether the elegant area-minimizing principle of the foam model is at play in this type of system.

ACKNOWLEDGMENTS

We thank our colleague and collaborator Z. B. Hu for the particle synthesis and for providing us with excellent sample material over the past years. Financial support from the Swiss National Science Foundation (200021_132128) and from the ACS Petroleum Research Fund (PRF 50603-DNI7) is gratefully acknowledged. We also thank Primoz Ziherl for helpful discussions.

[1] R. Pelton, Adv. Colloid Interface Sci. **85**, 1 (2000).
[2] J. J. Lietor-Santos, B. Sierra-Martin, R. Vavrin, Z. B. Hu, U. Gasser, and A. Fernandez-Nieves, Macromolecules **42**, 6225 (2009).
[3] A. Fernandez-Nieves, A. Fernandez-Barbero, B. Vincent, and F. J. d. l. Nieves, Macromolecules **33**, 2114 (2000).
[4] A. Fernandez-Nieves, A. Fernandez-Barbero, and F. J. d. l. Nieves, J. Chem. Phys. **115**, 7644 (2001).
[5] A. Fernandez-Nieves, A. Fernandez-Barbero, B. Vincent, and F. J. d. l. Nieves, J. Chem. Phys. **119**, 10383 (2003).
[6] B. R. Saunders and B. Vincent, Adv. Colloid Interface Sci. **80**, 1 (1999).
[7] D. J. Beebe, J. S. Moore, J. M. Bauer, Q. Yu, R. H. Liu, C. Devadoss, and B.-H. Jo, Nature (London) **404**, 588 (2000).
[8] S. V. Vinogradov, T. K. Bronich, and A. V. Kabanov, Adv. Drug Delivery Rev. **54**, 135 (2002).
[9] M. J. Serpe, J. Kim, and L. A. Lyon, Adv. Mater. **16**, 184 (2004).
[10] L. A. Lyon and A. Fernandez-Nieves, Annu. Rev. Phys. Chem. **63**, 25 (2012).
[11] D. M. Heyes and A. C. Branka, Soft Matter **5**, 2681 (2009).
[12] D. Paloli, P. S. Mohanty, J. J. Crassous, E. Zaccarelli, and P. Schurtenberger, Soft Matter **9**, 3000 (2013).
[13] S. M. Hashmi and E. R. Dufresne, Soft Matter **5**, 3682 (2009).
[14] J. R. Seth, L. Mohan, C. Locatelli-Champagne, M. Cloitre, and R. T. Bonnecaze, Nat. Mater. **10**, 838 (2011).
[15] D. Gottwald, C. N. Likos, G. Kahl, and H. Löwen, Phys. Rev. Lett. **92**, 068301 (2004).
[16] U. Gasser, B. Sierra-Martin, and A. Fernandez-Nieves, Phys. Rev. E **79**, 051403 (2009).
[17] U. Gasser and A. Fernandez-Nieves, Phys. Rev. E **81**, 052401 (2010).
[18] T. Hellweg, C. D. Dewhurst, E. Brueckner, K. Kratz, and W. Eimer, Colloid Polym. Sci. **278**, 972 (2000).
[19] P. S. Mohanty and W. Richtering, J. Phys. Chem. B **112**, 14692 (2008).
[20] G. R. Deen and T. T. Lee, Polym. Bull. **69**, 827 (2012).
[21] P. Bolhuis and D. Frenkel, J. Chem. Phys. **106**, 666 (1997).
[22] S. Pronk and D. Frenkel, J. Chem. Phys. **110**, 4589 (1999).
[23] P. N. Pusey, W. van Megen, P. Bartlett, B. J. Ackerson, J. G. Rarity, and S. M. Underwood, Phys. Rev. Lett. **63**, 2753 (1989).
[24] A.-P. Hynninen and M. Dijkstra, Phys. Rev. E **68**, 021407 (2003).
[25] P. Ziherl and R. D. Kamien, Phys. Rev. Lett. **85**, 3528 (2000).
[26] P. Ziherl and R. D. Kamien, J. Phys. Chem. B **105**, 10147 (2001).
[27] X. Wu, R. H. Pelton, A. E. Hamielec, D. R. Woods, and W. McPhee, Colloid Polym. Sci. **272**, 467 (1994).
[28] T. G. Mason and M. Y. Lin, Phys. Rev. E **71**, 040801 (2005).
[29] H. Senff and W. Richtering, J. Chem. Phys. **111**, 1705 (1999).
[30] A. Bergamaschi, C. Broennimann, E. Eikenberry, B. Henrich, M. Kobas, P. Kraft, and B. Schmitt, in *The 16th International Workshop on Vertex Detectors* (Proceedings of Science, Lake Placid, NY, 2007).
[31] M. Stieger, J. Pedersen, P. Lindner, and W. Richtering, Langmuir **20**, 7283 (2004).
[32] M. Stieger, W. Richtering, J. Pedersen, and P. Lindner, J. Chem. Phys. **120**, 6197 (2004).
[33] J. J. Lietor-Santos, U. Gasser, R. Vavrin, Z. B. Hu, and A. Fernandez-Nieves, J. Chem. Phys. **133**, 034901 (2010).
[34] J. K. Percus and G. J. Yevick, Phys. Rev. **110**, 1 (1958).
[35] U. Gasser, J. Phys.: Condens. Matter **21**, 203101 (2009).
[36] B. J. Ackerson, S. E. Paulin, B. Johnson, W. van Megen, and S. Underwood, Phys. Rev. E **59**, 6903 (1999).
[37] S. Auer and D. Frenkel, Nature (London) **413**, 711 (2001).
[38] S. Auer and D. Frenkel, Phys. Rev. Lett. **91**, 015703 (2003).
[39] W. Loose and B. J. Ackerson, J. Chem. Phys. **101**, 7211 (1994).
[40] S. Hendricks and E. Teller, J. Chem. Phys. **10**, 147 (1942).